ACCSCIENCE PUBLISHING

International Journal of Bioprinting

RESEARCH ARTICLE

3D-printable alginate-MoS_2-AgNW hydrogel bioink for dual-mode wearable capacitive biosensors

Suraj Shinde[1†], Kang Hyeon Kim[1,2†], Omkar Pawar[3], Omkar A. Patil[3], Sooman Lim[3], and Han Eol Lee[1,2,4*]

[1]Division of Advanced Materials Engineering, Jeonbuk National University, Jeonju-si, Jeonbuk State, South Korea

[2]Division of Electronics and Information Engineering, Jeonbuk National University, Jeonju-si, Jeonbuk State, South Korea

[3]Department of Flexible and Printable Electronics, LANL-JBNU Engineering Institute, Jeonbuk National University, Jeonju, South Korea

[4]Department of JBNU-KIST Industry-Academia Convergence Research, Jeonbuk National University, Jeonju-si, Jeonbuk State, South Korea

(This article belongs to the *Special Issue: 3D-Printed Biomedical Devices*)

Abstract

The advancement of bioinks capable of enabling multifunctional, skin-conformal sensing platforms is essential for the next generation of wearable health monitoring systems. In this study, we present a 3D-printed, dual-mode biosensor fabricated using a composite hydrogel ink comprising sodium alginate, exfoliated molybdenum disulfide nanosheets (MoS_2NSs), silver nanowires (AgNWs), and Ca^{2+} crosslinkers. This bioink enables reliable extrusion-based printing on flexible substrates, forming wearable, conductive, and mechanically robust sensor architectures. The resulting soft sensor exhibits high-sensitivity capacitive touch sensing with fast response times and excellent mechanical repeatability under dynamic loading conditions. Furthermore, the device allows for real-time monitoring of sweat rate in response to constant humidity and perspiration levels. The synergistic integration of 2D MoS_2NSs and 1D AgNWs significantly improves electrical conductivity and mechanical durability, without compromising printability or hydration compatibility. The demonstrated dual-sensing functionality and scalable fabrication strategy underscore the potential of this platform for low-cost, customizable applications in wearable healthcare, fitness tracking, and human-machine interfaces.

Keywords: 3D bioprinting; Alginate hydrogel; Capacitive touch sensing; Sweat rate monitoring; Flexible sensors; Skin-interfaced devices

1. Introduction

Recent advances in wearable electronics have enabled the development of skin-conformal, soft sensors capable of real-time physiological monitoring, offering transformative potential in personalized healthcare and human-machine interfaces.[1-4] Among the various biosensing modalities, simultaneous monitoring of tactile stimuli[5, 6]

†These authors contributed equally to this work

***Corresponding author:**
Han Eol Lee
(haneol@jbnu.ac.kr)

Citation: Shinde S, Kim KH, Pawar O Patil OA Lim S, Lee HE. 3D-printable alginate-MoS_2-AgNWs hydrogel bioink for dual-mode wearable capacitive biosensors. *Int J Bioprint*. 2025;11(5):301-314. doi: 10.36922/IJB025290295

Received: July 18, 2025
Revised: August 14, 2025
Accepted: August 22, 2025
Published online: August 25, 2025

and sweat secretion[7,8] at the skin's surface provides critical insights into an individual's hydration status, psychological stress levels, and physical activity.[9-11] To realize these functions in epidermal devices, sensors must meet specific requirements—including mechanical flexibility, biocompatibility, and stable signal transduction—under conditions of repeated mechanical deformation and prolonged skin contact.[12-14]

Hydrogel-based sensors have emerged as attractive platforms for skin-integrated electronics due to their high water content, intrinsic softness, and tunable mechanical properties.[15-17] Alginate, a naturally derived polysaccharide extracted from brown algae, is widely utilized in biomedical applications owing to its biocompatibility, gel-forming capability via divalent ion crosslinking, and excellent water retention properties.[18-21] These features make alginate a promising matrix material for soft hydrogel-based biosensors. However, the intrinsically insulating nature of alginate limits its application in electrically active devices, necessitating the incorporation of conductive nanomaterials to impart electronic functionality.[22,23] To overcome this limitation, recent research has explored the integration of conductive polymers, 1D and 2D nanomaterials, ionic compounds, liquid metals within hydrogel matrices to develop multifunctional and conductive composites, such as Poly(2,3-dihydrothieno-1,4-dioxin)-poly(styrenesulfonate) (PEDOT:PSS), metal nanoparticles, graphene oxide (GO), and carbon nanotubes (CNTs).[24] The integration of 1D and 2D nanomaterials and hydrogel matrices demonstrated great advances, such as an uncomplicated synthesis process, high electrical performance, mechanical reinforcement, flexibility, and biocompatibility.[25-28] However, hydrogel matrices dispersed with metal particles, conductive polymers, ionic compounds, and liquid metals presented disadvantages in various fields, such as degradation of mechanical strength, conductivity, toughness, deformability, and stability in a complex environment, which deteriorate their practical application as wearable devices.[29-31] Molybdenum disulfide (MoS_2), a prototypical 2D transition metal dichalcogenide (TMD), exhibits tunable semiconducting behavior, large specific surface area, and notable environmental stability.[32,33] When exfoliated into ultrathin nanosheets (NSs), MoS_2 enhances electronic coupling and provides capacitive characteristics within polymeric matrices. MoS_2 was also spotlighted as a humidity sensor with high sensitivity due to the presence of inherent defects. However, the pristine MoS_2 is not appropriate for a hydrogel filler with a monolithic sensor due to its low conductive properties.[34-36] Complementing this, silver nanowires (AgNWs) serve as highly conductive 1D fillers that create percolating networks for efficient charge transport, even under mechanical deformation.[37] Notably, both MoS_2NSs and AgNWs display favorable biocompatibility: MoS_2 exhibits low cytotoxicity and chemical stability, while AgNWs confer additional antibacterial functionality, mitigating the risk of microbial activity and skin irritation during prolonged use.[38-44] Despite significant advancements in nanocomposite hydrogel systems, most existing studies have focused on single-function sensors, and few have reported a single printable bioink formulation capable of supporting multimodal biosensing performance, such as both touch detection and hydration monitoring. In the case of the MoS_2 and AgNW, only a few studies have reported on a hydrogel, even a non-sensing application such as flame retardancy, wound healing patch, and flexible heater.[45-47] This limitation has constrained the development of versatile, skin-compatible platforms for integrated physiological assessment.

In this study, we report a printable nanocomposite ink composed of sodium alginate, MoS_2NSs, AgNWs, and Ca^{2+}, designed for extrusion-based 3D bioprinting. The combinations of MoS_2NSs and AgNWs featured enhanced conductive and carrier dynamics in the monolithic electrode-sensor system. The resulting nanocomposite bioink exhibits excellent rheological and structural properties for extrusion-based 3D printing on flexible substrates, while achieving high electrical conductivity and biocompatibility. Calcium-induced crosslinking reinforces the mechanical integrity of the alginate network and preserves hydration, which is critical for both skin comfort and ionic conduction. Using this printable bioink and a custom-designed bioprinting apparatus, we fabricated soft, flexible biosensors capable of dual-mode sensing: capacitive touch detection and real-time sweat rate monitoring. The printed devices demonstrate stable performance after bending and tensile strain, and maintain sensitivity in both ambient and on-body environments. The capacitive haptic sensor array displayed a capacitance difference at 10-8 mm from the sensor to the bare hand, indicating the high sensitivity of the system as a touch sensor. The integration of multifunctionality, high sensitivity, mechanical robustness, and printability highlights the potential of nanocomposite hydrogel materials for next-generation soft electronic devices.

2. Materials and methods

2.1. Materials

Sodium alginate, calcium chloride ($CaCl_2$), bulk MoS_2 powder, sodium chloride (NaCl), AgNWs in ethanol suspension (diameter: ~40 nm; length: ~30 μm), styrene-ethylene-butylene-styrene (SEBS), phosphate-buffered saline (PBS), and toluene were purchased from Sigma-

Aldrich (USA). All reagents were used as received without further purification.

2.2. Preparation of exfoliated MoS_2 nanosheets

The MoS_2NSs were synthesized via a liquid-phase exfoliation method.[48] Briefly, 100 mg of bulk MoS_2 powder was dispersed in 100 mL of an ethanol/deionized (DI) water mixture (volume ratio: 40:50 v/v). The suspension was sonicated in a bath sonicator (Branson Ultrasonics, United States of America [USA]) for 12 h at room temperature. Following sonication, the dispersion was centrifuged at 4000 rpm for 30 min (5810 R, Eppendorf, Germany) to remove unexfoliated particles. The supernatant containing few-layer MoS_2 nanosheets was collected and stored at 4°C for subsequent use.

2.3. Fabrication of alginate/MoS_2NS/AgNW composite ink

A 2 wt% sodium alginate solution was prepared by dissolving alginate in DI water under continuous overhead stirring at 600 rpm for 3 h until a clear, homogeneous gel was obtained. Exfoliated MoS_2NSs were added at varying concentrations (2, 3, and 4 wt% relative to alginate mass), followed by the addition of 0.1 wt% AgNWs. The mixture was further homogenized using magnetic stirring for 1 h to achieve a uniform composite ink. The final ink formulation was denoted as AAM.

2.4. 3D printing of soft sensor array

The AAM ink was transferred into a 5 mL syringe barrel equipped with a 26-gauge nozzle (inner diameter: 210 μm). Extrusion-based 3D printing was conducted using a custom-built bioprinter (Dr. INVIVO 4D6, ROKIT Healthcare, South Korea) with a pneumatic pressure of 700 kPa and a printing speed of 1 mm/s. The sensor patterns were deposited on flexible SEBS substrates (thickness: 200 μm) affixed to a heated bed maintained at 40°C. Sensor geometries were designed using Autodesk 3ds Max 2024 and sliced with Dr. INVIVO Slicer (ROKIT Healthcare, South Korea). Printed structures were crosslinked post-printing by immersion in 10 mM $CaCl_2$ solution for 30 min, followed by rinsing with DI water to remove unbound calcium ions.

2.5. Material characterization

Morphological features were characterized using field-emission scanning electron microscopy (FE-SEM; Hitachi S-4800, Japan) equipped with energy-dispersive X-ray spectroscopy (EDS) for elemental mapping. Raman spectroscopy (Horiba, Japan) was performed using a 532 nm excitation laser to analyze the structural properties of the AAM composite. Thermogravimetric analysis (TGA) was conducted using a TGA Q550 system (TA Instruments, USA) in a nitrogen atmosphere from room temperature to 500°C at a heating rate of 10°C/min.

2.6. Electrical and sensing performance evaluation

Sheet resistance measurements were carried out using a standard four-point probe setup (Keithley, USA). Capacitive touch sensing performance was evaluated via a customized setup where a human finger applied periodic touch stimuli (~10 kPa), while the electrical signals were recorded using an impedance analyzer (Keysight E4990A, USA). To assess moisture sensitivity, humidity-controlled tests were performed in an environmental chamber with relative humidity (RH) at 60%. For on-skin measurements, the sensor was attached to the volar forearm and operated under natural skin conditions (surface temperature ≈ 35°C) for up to 8 h while monitoring capacitive touch and sweat rate signals.

2.7. Statistical analysis

All experiments were conducted in triplicate unless otherwise indicated. Data are expressed as mean ± standard deviation. Statistical analyses and graphical visualizations were performed using OriginPro 2025 (OriginLab Corporation, USA) and MATLAB R2022b (MathWorks, USA).

3. Results and discussion

3.1. Fabrication of AAM-based conductive sensor array

The fabrication process of the alginate-based sensor array incorporating MoS_2NSs and AgNWs is schematically illustrated in **Figure 1**. Bulk MoS_2 powder was exfoliated via sonication in an ethanol/water solvent mixture to yield few-layer MoS_2NSs. The NSs and AgNWs were then homogeneously dispersed in a sodium alginate solution to formulate a printable, hydrogel-based conductive ink (**Figure 1a**). This composite ink was extruded using a syringe-assisted 3D bioprinter onto flexible SEBS substrates in a predefined sensor array geometry (**Figure 1b**). The inset in **Figure 1b** confirms stable extrusion through a 260 μm nozzle and high printing fidelity at the microscale. Post-printing, the structures were immersed in a 10 mM $CaCl_2$ bath, enabling ionic crosslinking of the alginate matrix and improving mechanical robustness. The resulting device consisted of a 10 × 10 array of 5 × 5 mm square sensor pads arranged with 7 mm spacing, forming a soft, conformal surface suitable for skin integration (**Figure 1c**).

3.2. Morphological and structural characterization

Figure 2a presents the morphological, structural, and compositional analysis of the AAM composite. The field-emission SEM image reveals the surface topology of the printed hydrogel film, exhibiting a continuous

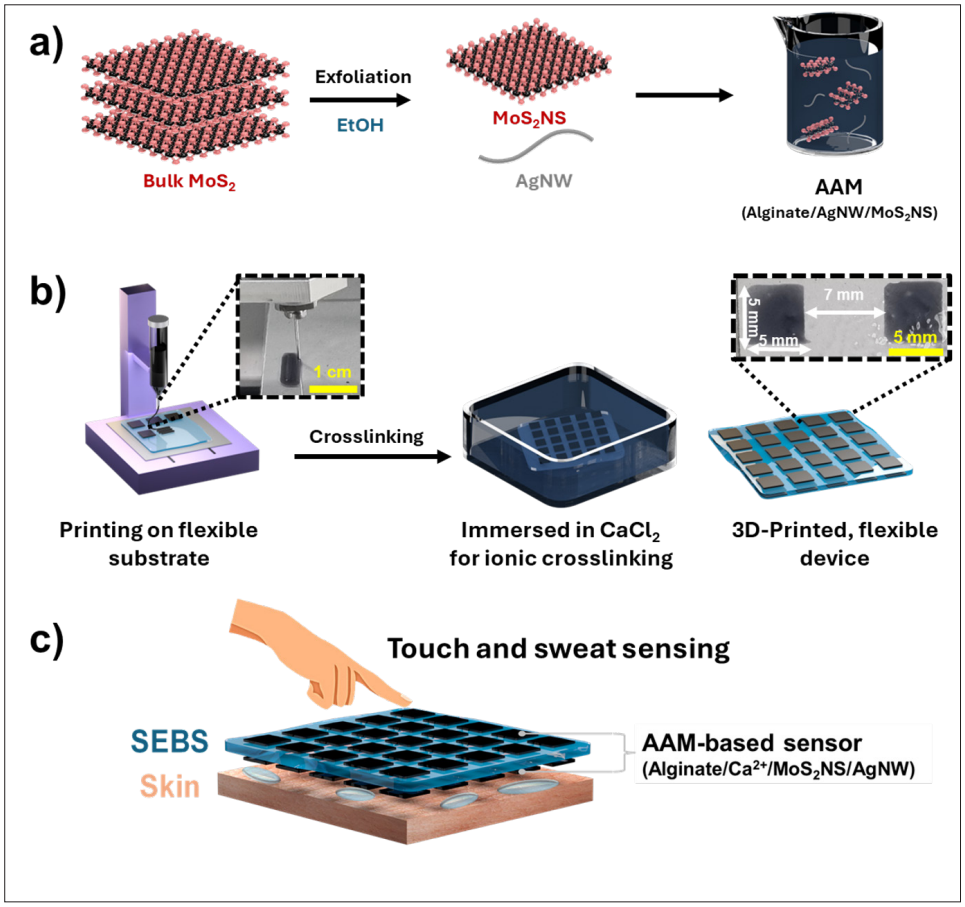

Figure 1. AAM-based sensor fabrication and sensing. (a) Schematic fabrication processes of AAM-based bioink. (b) 3D printing of AAM bioink on flexible SEBS substrate, and final crosslinking process. Optical images of printed sensor arrays (5 × 5 mm pads, 7 mm spacing) on flexible SEBS. (c) 3D illustration of dual-mode wearable capacitive biosensors with touch and sweat sensing. Abbreviations: AAM (Alginate-AgNWs-MoS_2NS), AgNW (silver nanowire), MoS_2NS (Molybdenum disulfide nanosheet) .

polymeric network embedded with nanoscale features. The magnified view confirms the incorporation of exfoliated MoS_2 nanosheets and interconnected AgNWs uniformly dispersed within the alginate matrix, forming a conductive percolation pathway. Additional high-resolution SEM images of the individual MoS_2NSs and AgNWs are provided in **Figure S1**, further validating their representative morphology and dispersion quality prior to composite formulation. **Figure 2b** displays an SEM image of the crosslinked AAM composite, which demonstrates a dense and integrated microstructure with uniformly distributed nanofillers. Elemental mapping via energy-dispersive X-ray spectroscopy (EDS) confirms the successful incorporation of all key constituent elements of Mo, S, Ag, Na, Ca, and Cl, corresponding to the AAM composition. **Figure 2c** presents the Raman spectra of the composite inks, highlighting characteristic vibrational features of MoS_2 within the hydrogel matrix. Both alginate/MoS_2NS and alginate/MoS_2NS/AgNW formulations exhibit two prominent peaks corresponding to the $E_{12}g$ (~383 cm^{-1}) and A_1g (~410 cm^{-1}) modes of MoS_2, indicative of in-plane and out-of-plane phonon vibrations, respectively. Notably, the AgNW-integrated composite (blue curve) exhibits an enhanced Raman signal intensity, suggesting improved NS dispersion and interfacial interactions between MoS_2 and the embedded AgNW network. These findings support the formation of a homogeneous, hybrid conductive matrix suitable for next-generation sensing applications. The TGA analysis was conducted to assess the thermal stability and decomposition behavior of the AAM ink and its individual components, MoS_2NSs and AgNWs, as displayed in **Figure 2d**. The TGA profile of MoS_2NSs demonstrates excellent thermal stability with negligible weight loss up to 500°C, confirming its inert behavior under the specified conditions. Similarly, AgNWs exhibit minimal mass change throughout the temperature range, reflecting their

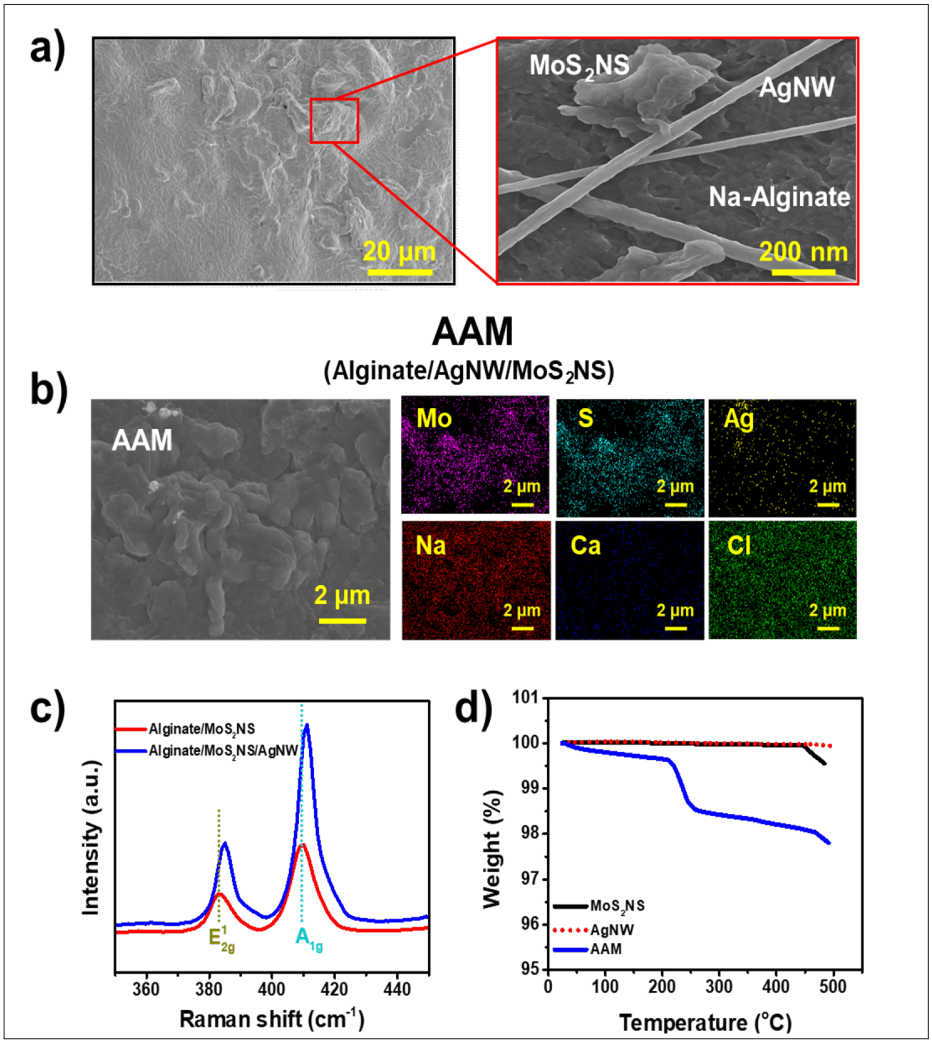

Figure 2. Material analysis of AAM component (a) SEM image of AAM composite, showing uniform distribution of nanoscale fillers. (b) EDS mapping images of Mo, S, Ag, Na, Ca, and Cl within the printed AAM matrix. (c) Raman spectra of Alginate/MoS_2NS and Alginate/MoS_2NS/AgNW inks, showing enhanced signal intensity and peak definition upon AgNW inclusion. (d) TGA results of MoS_2NS, AgNW, and AAM. Abbreviations: AAM (Alginate-AgNWs-MoS_2NS), AgNW (silver nanowire), MoS_2NS (Molybdenum disulfide nanosheet)

intrinsic high thermal stability and oxidation resistance at moderate temperatures. In contrast, the AAM composite exhibits a multistep decomposition profile. An initial minor mass loss below 150°C is attributed to the evaporation of absorbed moisture. A significant weight reduction between ~200°C and 300°C corresponds to thermal degradation of the alginate matrix via glycosidic bond cleavage and the release of volatile products. Above 300°C, a gradual mass loss occurs, likely associated with decomposition of residual carbonaceous species originating from alginate. The remaining mass beyond 500°C predominantly corresponds to inorganic residues, including MoS_2NSs and AgNWs. Collectively, these results confirm the enhanced thermal stability of the AAM composite due to the incorporation of thermally resilient MoS_2 and AgNW nanofillers and validate the material's structural integrity for practical and environmental applications in wearable electronics.

3.3. Influence of MoS_2NS/AgNW content on rheology, printability, and conductivity

Figure 3 presents the influence of conductive filler concentration on the electrical and rheological properties of the alginate-based composite inks. To minimize the deterioration of the mechanical properties of a hydrogel, nanomaterials within the hydrogel have to be minimally dispersed.[29] As displayed in Figure 3a, the electrical conductivity of the composites markedly increases with higher nanofiller loadings, particularly for the alginate/MoS_2NS/AgNW formulation. Notably, the inclusion of AgNWs into the MoS_2NS matrix results in a pronounced

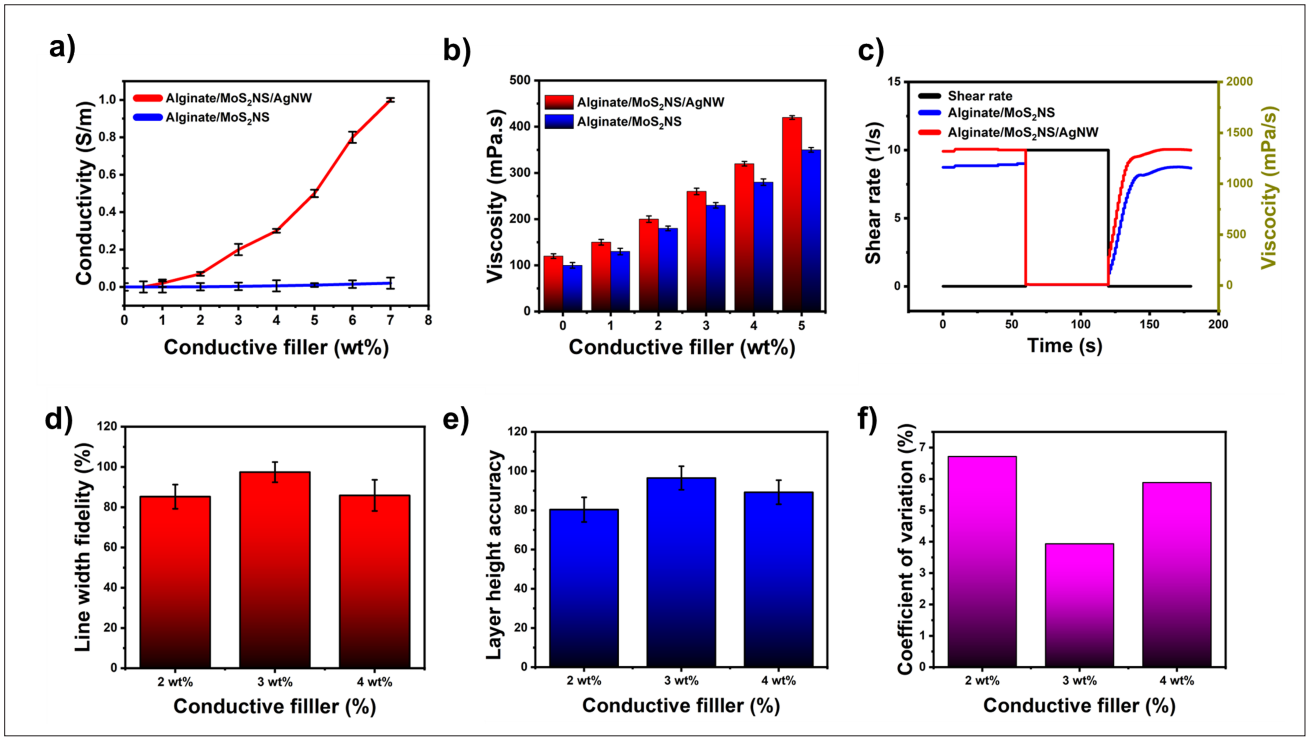

Figure 3. Electrical and rheological analysis and 3D printing optimization of AAM (a) Electrical conductivity of bioink according to nanofiller contents, demonstrating synergistic improvement with MoS_2NS and AgNW co-loading. (b) Viscosity profile of bioinks with increasing MoS_2NS/AgNW. (c) Shear-thinning behavior of both composite formulations. (d) Line width fidelity (%). (e) Layer height accuracy (%). (f) Extrusion stability over 180 s continuous printing. The replicates for error bar is (a,b) $n = 5$, (d,e) $n = 3$. Abbreviations:AAM (Alginate-AgNWs-MoS_2NS), AgNW (silver nanowire), MoS_2NS (Molybdenum disulfide nanosheet)

enhancement in conductivity, especially beyond 2 wt%, reaching values approaching 1 S/m at 7 wt%. In contrast, composites containing only MoS_2NSs exhibit minimal improvement, underscoring the synergistic effect of combining 2D MoS_2NSs with 1D AgNWs to form an efficient percolated conductive network. The results indicate AgNW rapidly improved the conductivity of alginate/MoS_2NS with the additional lower ratio of materials than MoS_2NS to prevent the unequal dispersion of nanomaterials (**Table 1**). The viscosity profiles presented in **Figure 3b** indicate a progressive increase in viscosity with increasing filler concentration for both composite types. The AgNW-integrated inks consistently exhibit slightly higher viscosities across all concentrations, which is attributed to enhanced mechanical entanglement and improved interfacial interactions within the hybrid network. Further rheological analysis under applied shear reveals that both formulations demonstrate characteristic shear-thinning behavior, a desirable feature for extrusion-based 3D printing (**Figure 3c**). The alginate/MoS_2NS/AgNW formulation maintains a higher viscosity across all shear rates, reflecting stronger internal network interactions facilitated by the presence of AgNWs. Importantly, both ink systems exhibit good structural recovery after shear removal, confirming their suitability for precise, layer-by-layer deposition during printing. **Figure S2** displays optical microscopy images of printed lines fabricated using inks with different filler concentrations (2, 3, and 4 wt%). The 3 wt% formulation produces the most uniform and well-defined printed features, representing an optimal balance between flow stability and spatial resolution. At 2 wt%, the printed lines appear weakly defined and underdeveloped, while at 4 wt%, irregular extrusion and occasional nozzle clogging are observed. These defects are attributed to excessive filler content, which negatively impacts the ink's flowability and extrusion consistency. Taken together, these results illustrate the critical importance of optimizing nanofiller concentrations to achieve stable printability, reliable electrical performance, and appropriate rheological behavior. To quantitatively evaluate the printability of the composite inks, three printing quality metrics were assessed: line width fidelity, layer height accuracy, and extrusion stability. The line width fidelity, defined as the ratio of the measured to the designed width, was measured for inks containing 2, 3, and 4 wt% MoS_2NS/AgNWs. The optimal formulation (3 wt% MoS_2NS/AgNWs) achieved a

Table 1. Comparison of conductive hydrogel with different fillers

Study	Filler material	Matrix	Conductivity (S/cm)	Fracture energy (kJ/m²)	Printability (line width fidelity %)	Ref.
Li *et al.*	Polyaniline (PANI)	Polyacrylamide (PAAm) hydrogel	0.12	15.8	~90%	[25]
Yu *et al.*	PEDOT:PSS	Poly(vinyl alcohol) (PVA) hydrogel	0.093	12.4	~95%	[26]
Van Tam *et al.*	Phosphorus-doped graphene QDs + graphene	Alginate hydrogel	0.85	9.6	~92%	[28]
Shinde *et al.*	MoS_2NS and AgNWs	Alginate hydrogel	0.01	27.55	98.3%	This work

Abbreviations: AgNW (silver nanowire), MoS_2NS (Molybdenum disulfide nanosheet), PAAm (Polyacrylamide), PANI (Polyaniline), PEDOT:PSS (Poly(2,3-dihydrothieno-1,4-dioxin)-poly(styrenesulfonate)), PVA (Poly(vinyl alcohol))

fidelity of 98.3 ± 3.1%, significantly higher than 2 wt% (91.7 ± 6.4%) and 4 wt% (88.2 ± 9.5%) formulations (**Figure 3d**). Layer height accuracy followed a similar trend, with 3 wt% MoS_2NS/AgNWs producing heights within 98.7 ± 4.2% of the designed 150 μm, indicating excellent vertical stacking precision (**Figure 3e**). Extrusion stability was monitored by measuring instantaneous line width over a 180 s continuous print. The coefficient of variation (CV) for the 3 wt% formulation was only 3.9%, compared to 4.6% for 2 wt% and 5.1% for 4 wt%, confirming minimal fluctuation in extrusion flow. These results quantitatively validate the superior print fidelity, structural resolution, and extrusion consistency of the optimized bioink, aligning with the high-resolution features observed in **Figure 3f**. This optimized hydrogel ink enables high-resolution patterning, consistent extrusion, and superior electrical functionality, making it an excellent candidate for our capacitive biosensor.

3.4. Mechanical properties of AAM composite

Figure 4 illustrates the mechanical performance of the AAM composite under both tensile and cyclic loading conditions. As presented in **Figure 4a**, photographic images of the printed hydrogel specimen demonstrate its high flexibility and stretchability when subjected to uniaxial elongation, transitioning smoothly from a relaxed to an extended state. This behavior confirms the excellent mechanical compliance of the material, which is essential for integration into wearable sensor platforms. The tensile stress–strain curves presented in **Figure 4b** indicate that both alginate/MoS_2NS and alginate/MoS_2NS/AgNW composites undergo similar elastic deformation up to approximately 10%. The incorporation of AgNWs yields a modest but consistent increase in mechanical strength, suggesting that AgNWs contribute incrementally to mechanical reinforcement without significantly compromising the innate extensibility of the hydrogel matrix (**Table 1**). **Figure 4c** displays the results of cyclic tensile testing, performed to assess the mechanical durability of the composites under repeated mechanical stress. Over 20 consecutive loading/unloading cycles, both formulations retain their stress-bearing capabilities, with the AgNW-reinforced AAM sample consistently exhibiting higher stress levels than its MoS_2-only counterpart. This indicates improved mechanical resilience and fatigue resistance conferred by the hybrid nanofiller network, featuring an essential characteristic for reliable operation in dynamic, body-mounted environments. The effect of crosslinking density on mechanical stiffness is investigated in **Figure 4d**, where increasing concentrations of $CaCl_2$ solution produced a nearly linear increase in compressive stress. This observation confirms that the ionic crosslinking facilitated by Ca^{2+} can be employed to modulate the mechanical properties of the hydrogel systematically. Such tunability provides a versatile strategy for tailoring the composite's softness or rigidity depending on the specific application or anatomical site of deployment.[48] Collectively, these findings validate that the AAM hydrogel composite exhibits robust mechanical integrity, high deformability, and enhanced toughness. The combined effects of 1D/2D nanofiller reinforcement and controllable ionic crosslinking provide a favorable mechanical profile, establishing the AAM composite as a promising candidate material for flexible and skin-compatible biosensing devices.

3.5. Capacitive touch sensing performance

The capacitive sensing performance of the AAM-based sensor was systematically evaluated under varying mechanical loading and proximity conditions, as presented in **Figure 5**. As displayed in **Figure 5a**, a progressive increase in capacitance was observed with increasing applied normal force ranging from 1 to 10 N, confirming the pressure-sensitive nature of the sensor. The touch sensitivity of the AAM-based sensor was determined from the slope of the normalized capacitance change (ΔC/

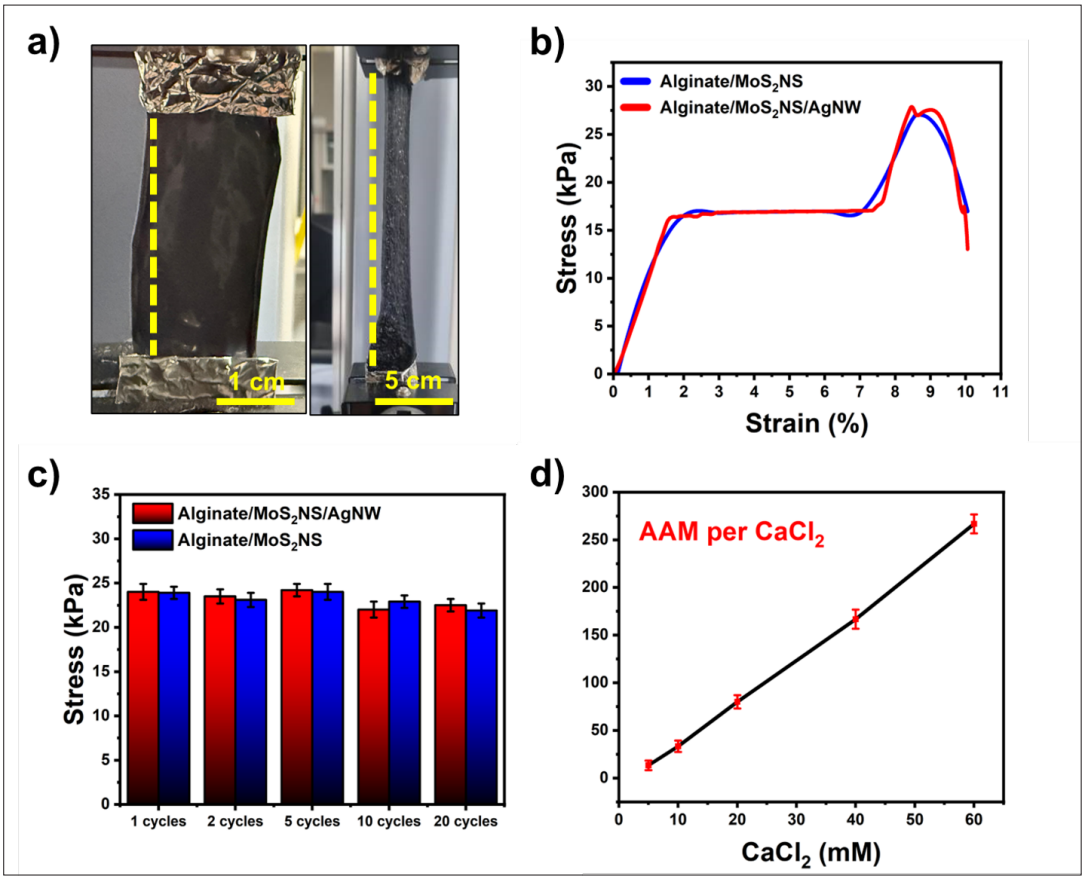

Figure 4. Mechanical properties of AAM-based hydrogel. (a) Optical images of AAM composite, featuring mechanical flexibility and elongation capability. (b) Tensile stress-strain profiles of alginate/MoS_2NS and AAM composites. (c) Cyclic tensile testing results over 20 loading/unloading cycles confirm mechanical durability ($n = 5$). (d) Compressive strength as a function of $CaCl_2$ concentration, featuring tunability of hydrogel stiffness through crosslinker variation ($n = 5$). AAM (Alginate-AgNWs-MoS_2NS), AgNW (silver nanowire), MoS_2NS (Molybdenum disulfide nanosheet)

C_0) versus applied pressure in the low-pressure range (10–50 kPa, corresponding to 1–5 N in **Figure 5a**). The calculated value was ≈ 0.15 kPa^{-1}, which is comparable to or higher than those reported for similar hydrogel-based capacitive sensors.[49] Repetitive finger-touch experiments were conducted to assess signal stability and repeatability under dynamic input conditions. As illustrated in **Figure 5b**, distinct and reproducible capacitive peaks were consistently generated over multiple touch-release cycles. Each mechanical stimulus resulted in a sharp increase in capacitance followed by rapid signal recovery upon unloading, indicating high temporal resolution and signal fidelity. This behavior is attributed to the elastic recoverability of the alginate hydrogel matrix and the robustness of the embedded MoS_2NS/AgNW conductive network. To further assess proximity sensing capability, controlled finger approaches were performed at varying distances (9–10, 7–5, and 4–2 mm) from the sensor surface. As displayed in **Figure 5c**, a gradual increase in capacitance was recorded as the distance decreased, culminating in a sharp peak upon direct contact. These results validate the sensor's efficacy in near-field proximity detection, enabling pre-contact recognition for potential human-machine interface applications. Spatial pressure distribution mapping was demonstrated using a 5 × 5 electrode array configuration (**Figure 5d**). The corresponding heatmap reflects localized capacitance changes across the array when mechanical pressure was selectively applied. Each coloured cell represents the capacitive response of a specific electrode pair subjected to pressure input. The gradient from blue to red denotes increasing signal magnitude, with electrodes at positions (1,1) and (2,1) exhibiting notably higher capacitance values. These elevated readings indicate focused mechanical stimulus in the lower-left region, further confirming the system's spatial resolution. Collectively, these findings demonstrate that the AAM-based capacitive sensor is capable of both pressure and proximity detection with high spatial and temporal

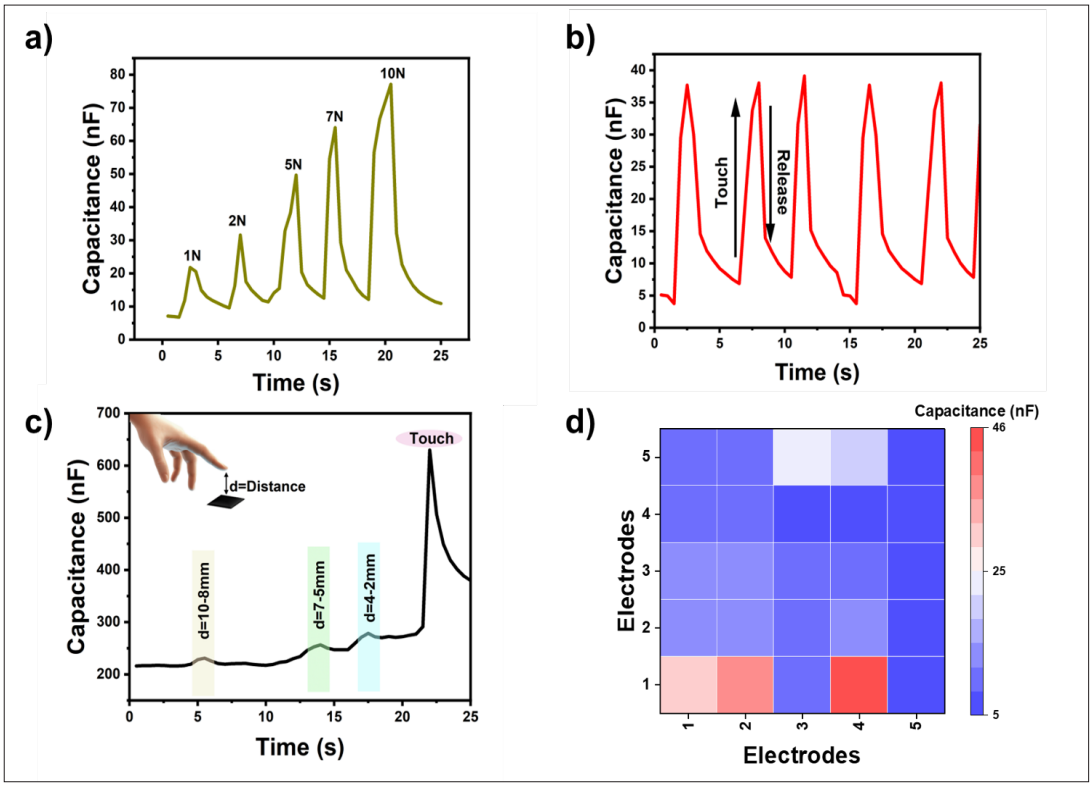

Figure 5. Pressure sensing performance of AAM-based sensor (a) Capacitance response of AAM sensor under increasing finger-applied forces (1–10 N). (b) Repetitive touch cycles display high signal fidelity and recovery. (c) Capacitance variation with proximity sensing (2–10 mm). (d) Heatmap generated by a 5 × 5 sensor array for spatial mapping, demonstrating multiple high-resolution touch localizations.

resolution. The integrated functionality renders the system highly applicable for use in wearable touch sensors and pressure-mapping technologies, where reliable detection of dynamic and localized stimuli is essential.

3.6. Hydration and sweat rate sensing

Sweat absorption into the hydrogel leads to a modification of its dielectric constant due to the presence of the aqueous phase. The electrolyte species present in sweat, including Na^+, Cl^-, and K^+, further accelerate the capacitance changes. This acceleration arises from the enhancement of ionic transport mechanisms provided by MoS_2NS to amplify the electrical response of the hydrogel-based sensor.[50-52] The capacitive response of the printed AAM sensor was investigated under varying sweat flow rates to evaluate its sensitivity to perspiration-related stimuli (**Figure 6**). In **Figure 6a**, the normalized capacitance change ($\Delta C/C_0$) exhibited a clear increasing trend with rising artificial sweat flow rates, ranging from 1.0 to 4.0 μL/min. This progressive signal enhancement indicates improved surface interaction between absorbed moisture and the conductive hydrogel interface under elevated moisture flux. The observed increase in signal amplitude and slope suggests that higher flow rates promote more effective electrolyte–electrode interactions and facilitate ion transport within the capacitive sensing interface. Specifically, the response amplitude increased from approximately 40% at a flow rate of 1.0 μL/min to over 130% at 4.0 μL/min, demonstrating the sensor's high sensitivity to variations in fluid dynamics. The corresponding response factor (K) (**Figure 6b**) displayed a near-linear correlation with sweat speed, confirming the sensor's quantitative responsiveness to dynamic hydration levels. The upward trend in K values is attributed to enhanced dielectric interactions at the hydrogel-moisture interface, facilitated by the porous and highly hydrophilic structure of the composite matrix. Further evaluation of electrolyte specificity was performed by comparing sensor responses to deionized water, artificial sweat, and NaCl solutions with varying ionic strengths (1, 10, and 100 mM), as depicted in **Figure 6c**. The resulting capacitance responses remained consistent across the different electrolyte types and concentrations, indicating that the sensor's humidity detection mechanism is governed predominantly by moisture content rather than ionic conductivity. This ionic insensitivity is advantageous for wearable monitoring, where sweat composition may fluctuate significantly over

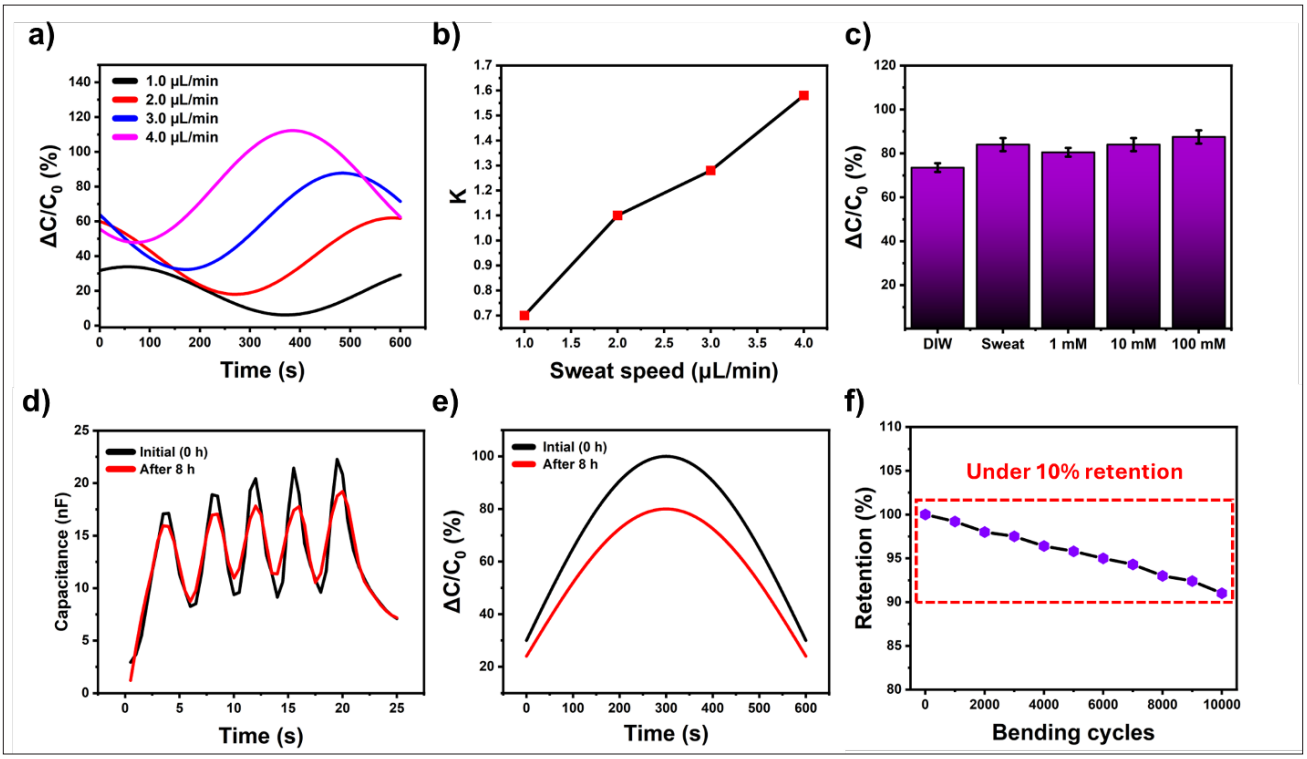

Figure 6. Sweat ion sensing results of AAM-based sensor. (a) Normalized capacitance change ($\Delta C/C_0$) with increasing artificial sweat rates (1.0–4.0 μL/min). (b) Response factor (K) as a function of sweat rate, displaying near-linear behavior. (c) Comparison of capacitance response in DI water, artificial sweat, and NaCl solutions of varying concentration, confirming moisture-dominant sensitivity (n = 5). (d) Capacitance variation over time during real-time wearable testing. The black line represents the initial capacitive response, while the red line indicates performance after 8 h of continuous wear. (e) Normalized capacitance change ($\Delta C/C_0$) over time under constant human sweat flow rate (3.0 μL/min), comparing initial state and after 8 h of on-skin wear. (f) Cyclic bending retention curve showing less than 10% degradation after 10000 cycles.

time due to physiological and environmental factors. Altogether, these results demonstrate that the AAM sensor is capable of real-time sweat rate monitoring with stable, reversible capacitive output.

3.7. Long-term stability and on-skin performance

To verify the applicability of the AAM-based dual-mode biosensor under realistic wearable conditions, extended-duration tests were conducted. For on-skin performance evaluation, the sensor was attached to the forearm and worn continuously during daily activities for over 8 h. During the 8 h continuous on-skin test, the device operated at a constant skin temperature (~35°C). Despite this thermal exposure, baseline signals remained stable, and the device displayed only moderate amplitude reduction (~33%), confirming minimal performance drift at physiological temperatures (**Figure 6d**). Long-term sweat rate monitoring stability was also examined under a constant sweat flow rate (3.0 μL/min) for 8 h. The normalized capacitance change ($\Delta C/C_0$) decreased by ~20%, yet the waveform shape and periodicity remained consistent (**Figure 6e**), confirming robust hydration sensing performance during extended operation.

Additionally, mechanical durability under repetitive deformation was assessed by cyclic bending tests (radius ≈ 5 mm) up to 10000 cycles. The device retained ~90% of its initial signal response after the full cycle count (**Figure 6f**), indicating that the percolated MoS_2-AgNW conductive network within the alginate matrix remains stable under prolonged dynamic loading. Collectively, these findings demonstrate that the AAM-based biosensor maintains functional stability and durability in dynamic, skin-mounted environments, underscoring its potential for practical wearable healthcare and human-machine interface applications.

4. Conclusion

In this study, we developed and demonstrated a 3D-printed, dual-mode wearable biosensor based on a nanocomposite hydrogel ink composed of sodium alginate, exfoliated MoS_2NSs, AgNWs, and Ca^{2+} as ionic crosslinkers. The

composite ink exhibited excellent rheological properties suitable for extrusion-based printing and enabled the fabrication of soft, skin-conformal sensor arrays with high structural fidelity on flexible SEBS substrates. Comprehensive morphological and spectroscopic analyses confirmed the uniform dispersion of MoS_2NSs and AgNWs within the alginate matrix, forming a robust, percolating conductive network. The synergistic combination of 2D-MoS_2 and 1D-Ag nanowires led to enhanced electrical conductivity, carrier dynamics, and mechanical stability, while maintaining the hydrophilic and biocompatible nature of the hydrogel scaffold. The optimized formulation with 3 wt% MoS_2NS/AgNW provided the best balance between printability, conductivity, and viscoelastic control. The resulting AAM sensors demonstrated reliable capacitive performance in response to both mechanical and hydration stimuli. The device exhibited pressure-sensitive and proximity-dependent capacitance changes, with high spatial and temporal resolution in a 5 × 5 electrode array configuration. Moreover, the sensor exhibited strong responsiveness to varying sweat flow rates, with signal intensity increasing proportionally with moisture flux, and remained functionally robust across a wide range of ionic concentrations.

The capacitive haptic sensor array demonstrated a capacitance difference of 10-8 mm from the sensor to the bare hand, highlighting the high sensitivity of the system as a touch sensor. This confirms that the capacitive sensing mechanism is primarily driven by hydration level rather than ion concentration, making it highly suitable for wearable sweat monitoring. Overall, the proposed AAM-based sensor platform offers a low-cost, scalable solution for dual-mode biosensing in healthcare, fitness tracking, and human-machine interface applications. This dual-functional sensor platform offers broad application potential in healthcare monitoring for hydration and stress levels, fitness tracking, prosthetics, and interactive wearable systems requiring simultaneous mechanical and perspiration sensing.

Acknowledgments

This work was supported by the National University Development Project at Jeonbuk National University in 2024.

Funding

Not applicable

Conflict of interest

The authors declare no conflicts of interest.

Author contributions

Conceptualization: Suraj Shinde
Data curation: Suraj Shinde, Omkar A. Patil
Formal analysis: Omkar Pawar
Funding acquisition: Han Eol Lee
Investigation: Han Eol Lee
Methodology: Suraj Shinde, Sooman Lim, Han Eol Lee
Resources: Suraj Shinde, Kang Hyeon Kim, Omkar Pawar
Supervision: Han Eol Lee
Validation: Kang Hyeon Kim, Han Eol Lee
Visualization: Kang Hyeon Kim
Writing–original draft: Suraj Shinde
Writing–review & editing: Han Eol Lee

Ethics approval and consent to participate

Not applicable

Consent for publication

Not applicable.

Availability of data

The authors confirm that the data supporting the findings of this study are available within the article and its Supplementary File. Raw data that support the findings of this study are available from the corresponding author, upon reasonable request.

References

1. Che Ab Rahman A, Lee B-J,Lim S. Optimizing polymethyl methacrylate (PMMA)-based stretchable microneedle arrays by vat photopolymerization for efficient drug loading. *Additive Manufacturing*. 2024;94:104472. doi: j.addma.2024.104472

2. Bae L K,Choi M K. Deformable Heat-Dissipation Materials for Smart E-Skin. *J Korean Inst Electr Electron Mater Eng*. 2025;38(1):21-32. doi: 10.4313/JKEM.2025.38.1.3

3. Jeong S, Hwang Y S, *et al.* Formation of Metal Mesh Electrodes via Laser Plasmonic Annealing of Metal Nanoparticles for Application in Flexible Touch Sensors. *J Korean Inst Electr Electron Mater Eng*. 2024;37(2):223-229. doi: 10.4313/JKEM.2024.37.2.15

4. Park J-C. Influence of Al Content on the Resonant Characteristics of Al-Mo Thin Film-Based SAW Devices. *Trans Electr Electron Mater*. 2025;38(1):65-71. doi: 10.4313/JKEM.2025.38.1.8

5. Khan F, Mubashir T, Ahmed K, Shahoor M, Mateen A, Lee S N,Ahmed T. Fabrication and Characterization of Carbon Nanotubes-Based Pressure Nanosensors: A Study

on Piezoresistive Behavior. *Trans Electr Electron Mater*. 2023;24(6):518-527.
doi: 10.1007/s42341-023-00472-6

6. Pawar O Y,Lim S. 3D-Printed piezoelectric nanogenerator with aligned graphitic carbon nitrate nanosheets for enhancing piezoelectric performance. *J Colloid Interface Sci*. 2024;654(Pt B):868-877.
doi: 10.1016/j.jcis.2023.10.105

7. Kim J H, Joe D J,Lee H E. Sweat-permeable electronic skin with a pattern of eyes for body temperature monitoring. *Micro Nano Syst Lett*. 2023;11(1):7
doi: 10.1186/s40486-023-00170-1

8. Shinde S, Kim K H, Park S Y, Kim J H, Kim J, Joe D J,Lee H E. Wearable sweat-sensing patches for non-invasive and continuous health tracking. *Sens Actuators Rep*. 2025;9:100265.
doi: 10.1016/j.snr.2024.100265

9. Son J, Bae G Y, *et al.* Cactus-Spine-Inspired Sweat-Collecting Patch for Fast and Continuous Monitoring of Sweat. *Adv Mater*. 2021;33(40):e2102740.
doi: 10.1002/adma.202102740.

10. Liang H R, Zhu M J, *et al.* Sweat-Enhanced Self-Adhesive Double-Network Hydrogel for Dynamic Skin Electrophysiology. *Acs Materials Letters*. 2024;6(11):4922-4931.
doi: 10.1021/acsmaterialslett.4c01748

11. Lyzwinski L, Elgendi M, Shokurov A V, Cuthbert T J, Ahmadizadeh C,Menon C. Opportunities and challenges for sweat-based monitoring of metabolic syndrome via wearable technologies. *Commun Eng-London*. 2023;2(1):48.
doi: 10.1038/s44172-023-00097-w

12. Yeon H, Lee H, *et al.* Long-term reliable physical health monitoring by sweat pore-inspired perforated electronic skins. *Sci Adv*. 2021;7(27):eabg8459
doi: 10.1126/sciadv.abg8459

13. Kim J H, Kim H, Jeong C K,Lee H E. 3D-Porous Structured Piezoelectric Strain Sensors Based on PVDF Nanocomposites. *J Sens Sci Technol*. 2022;31(5):307-311.
doi: 10.46670/jsst.2022.31.5.307.

14. Liu Y, Liu J, *et al.* Soft and elastic hydrogel-based microelectronics for localized low-voltage neuromodulation. *Nat Biomed Eng*. 2019;3(1):58-68.
doi: 10.1038/s41551-018-0335-6

15. Zhou P C, Zhang Z M, Mo F,Wang Y. A Review of Functional Hydrogels for Flexible Chemical Sensors. *Adv Sensor Res*. 2024;3(3):2300021.
doi: 10.1002/adsr.202300021

16. Shinde S, Patil O A, *et al.* Wearable sweat glucose monitoring patches enabled by double network hydrogel-MoS2/PEDOT: PSS nanocomposite. *Microchem J*. 2025;215:114309.
doi: 10.1016/j.microc.2025.114309

17. Morozkina S, Strekalovskaya U, Vanina A, Snetkov P, Krasichkov A, Polyakova V,Uspenskaya M. The Fabrication of Alginate-Carboxymethyl Cellulose-Based Composites and Drug Release Profiles. *Polymers (Basel)*. 2022;14(17):3604.
doi: 10.3390/polym14173604.

18. Jia J, Richards D J, *et al.* Engineering alginate as bioink for bioprinting. *Acta Biomater*. 2014;10(10):4323-4331.
doi: 10.1016/j.actbio.2014.06.034

19. Zhang W, Kuss M, Yan Y,Shi W. Dynamic Alginate Hydrogel as an Antioxidative Bioink for Bioprinting. *Gels*. 2023;9(4):312.
doi: 10.3390/gels9040312

20. Salesa B, Llorens-Gamez M,Serrano-Aroca A. Study of 1D and 2D Carbon Nanomaterial in Alginate Films. *Nanomaterials (Basel)*. 2020;10(2):206.
doi: 10.3390/nano10020206

21. Zhang Y, Li S, *et al.* Highly conductive and tough polyacrylamide/sodium alginate hydrogel with uniformly distributed polypyrrole nanospheres for wearable strain sensors. *Carbohydr Polym*. 2023;315:120953.
doi: 10.1016/j.carbpol.2023.120953

22. Huang J, Chen G, *et al.* Ultrafast and facile construction of programmable, multidimensional wrinkled-patterned polyacrylamide/sodium alginate hydrogels for human skin-like tactile perception. *Carbohydr Polym*. 2023;319:121196.
doi: 10.1016/j.carbpol.2023.121196

23. Shinde S,Lee H E. Wearable Strain Sensors via Tough and Conductive Hydrogel-Based MoS (2) Composites for Real-Time Motion Tracking. *ACS Omega*. 2025;10(23):25102-25110.
doi: 10.1021/acsomega.5c03752

24. Choudhury S, Deepak D, Bhattacharya G, McLaughlign J,Roy S S. MoS-Polyaniline Based Flexible Electrochemical Biosensor: Toward pH Monitoring in Human Sweat. *Macromol Mater Eng*. 2023;308(8):2300007.
doi: 10.1002/mame.202300007

25. Li L, Ai Z, Wu J, Lin Z, Huang M, Gao Y,Bai H. A robust polyaniline hydrogel electrode enables superior rate capability at ultrahigh mass loadings. *Nat Commun*. 2024;15(1):6591.
doi: 10.1038/s41467-024-50831-x

26. Yu J, Wan R, *et al.* 3D Printing of Robust High-Performance Conducting Polymer Hydrogel-Based Electrical Bioadhesive Interface for Soft Bioelectronics. *Small*. 2024;20(19):e2308778.
doi: 10.1002/smll.202308778

27. Lu Y Y, Yang G, *et al.* Stretchable graphene-hydrogel interfaces for wearable and implantable bioelectronics. *Nature Electronics*. 2023;7(1):51-65.
doi: 10.1038/s41928-023-01091-y

28. Van Tam T, Chandra Bhamu K, Jae Kim M, Gu Kang S, Suk Chung J, Hyun Hur S,Mook Choi W. Engineering

phosphorous doped graphene quantum dots decorated on graphene hydrogel as effective photocatalyst and high-current density electrocatalyst for seawater splitting. *Chem Eng J*. 2024;480:148190.
doi: 10.1016/j.cej.2023.148190

29. Peng Q Y, Chen J S, *et al.* Recent advances in designing conductive hydrogels for flexible electronics. *Infomat*. 2020;2(5):843-865.
doi: 10.1002/inf2.12113

30. Fan Q, Zhang K, *et al.* Molecular Weight Tailored Hydrogen Bonding Networks in PVA/PEDOT: PSS: Decoupling the Conductivity-Flexibility Trade-Off for Robust Epidermal EMG Monitoring. *ACS Appl Mater Interfaces*. 2025;17(29):42278-42292.
doi: 10.1021/acsami.5c08001

31. Lo L W, Zhao J, Wan H, Wang Y, Chakrabartty S,Wang C. An Inkjet-Printed PEDOT:PSS-Based Stretchable Conductor for Wearable Health Monitoring Device Applications. *ACS Appl Mater Interfaces*. 2021;13(18):21693-21702.
doi: 10.1021/acsami.1c00537

32. Er E,Ates A K. Design of an electrochemical sensing platform based on MoS2-PEDOT:PSS nanocomposite for the detection of epirubicin in biological samples. *Microchem J*. 2023;189:108534.
doi: 10.1016/j.microc.2023.108534

33. Zhao C, Deng B, Chen G C, Lei B, Hua H, Peng H L,Yan Z M. Large-area chemical vapor deposition-grown monolayer graphene-wrapped silver nanowires for broad-spectrum and robust antimicrobial coating. *Nano Res*. 2016;9(4): 963-973.
doi: 10.1007/s12274-016-0984-2

34. Li P, Zhang D,Wu Z. Flexible MoS2 sensor arrays for high performance label-free ion sensing. *Sensors and Actuators A: Physical*. 2019;286:51-58.
doi: 10.1016/j.sna.2018.12.026

35. Kinnamon D, Ghanta R, Lin K-C, Muthukumar S,Prasad S. Portable biosensor for monitoring cortisol in low-volume perspired human sweat. *Sci Rep*. 2017;7(1):13312.
doi: 10.1038/s41598-017-13684-7

36. Shalini V, Harish S, Ikeda H, Hayakawa Y, Archana J,Navaneethan M. Investigating the effect of defect states and to enhance the electrical conductivity of p-type Vanadium-doped MoS2 for wearable thermoelectric application. *Journal of Alloys and Compounds*. 2023;960:170317.
doi: 10.1016/j.jallcom.2023.170317

37. Sha R,Bhattacharyya T K. MoS-based nanosensors in biomedical and environmental monitoring applications. *Electrochim Acta*. 2020;349:136370.
doi: 10.1016/j.electacta.2020.136370

38. Lee H G,Lee G. The Change of IV Characteristics by Gate Voltage Stress on Few Atomic Layered MoS 2 Field Effect Transistors. *J Korean Inst Electr Electron Mater Eng*. 2018;31(3):135-140.
doi: 10.4313/JKEM.2018.31.3.135

39. Sharma R, Kumar A, *et al.* Liquid Phase Exfoliation and Characterization of Few Layer MoS and WS Nanosheets as Channel Material in Field Effect Transistor. *Trans Electr Electron Mater*. 2023;24(2):140-148.
doi: 10.1007/s42341-023-00429-9

40. Choi S, Han S I, *et al.* Highly conductive, stretchable and biocompatible Ag-Au core-sheath nanowire composite for wearable and implantable bioelectronics. *Nat Nanotechnol*. 2018;13(11):1048-1056.
doi: 10.1038/s41565-018-0226-8

41. Ahn Y, Lee H, Lee D,Lee Y. Highly conductive and flexible silver nanowire-based microelectrodes on biocompatible hydrogel. *ACS Appl Mater Interfaces*. 2014;6(21):18401-18407.
doi: 10.1021/am504462f

42. Appel J H, Li D O, Podlevsky J D, Debnath A, Green A A, Wang Q H,Chae J. Low Cytotoxicity and Genotoxicity of Two-Dimensional MoS(2) and WS(2). *ACS Biomater Sci Eng*. 2016;2(3):361-367.
doi: 10.1021/acsbiomaterials.5b00467

43. Kaur J, Singh M, *et al.* Biological interactions of biocompatible and water-dispersed MoS(2) nanosheets with bacteria and human cells. *Sci Rep*. 2018;8(1):16386.
doi: 10.1038/s41598-018-34679-y

44. Mondal S, Kim S J,Choi C G. Honeycomb-like MoS(2) Nanotube Array-Based Wearable Sensors for Noninvasive Detection of Human Skin Moisture. *ACS Appl Mater Interfaces*. 2020;12(14):17029-17038.
doi: 10.1021/acsami.9b22915

45. Liu Y, Liu D, Xue Y, Sun H, Zhan X, Sun L,Kang K. How Advanced are Conductive Nanocomposite Hydrogels for Repairing and Monitoring Myocardial Infarction? *Int J Nanomedicine*. 2025;20(null):6777-6812.
doi: 10.2147/IJN.S503445

46. Chang C, Guan X, Lin J, Nie H, Zhou X, Xie X,Ye Y. MoS(2) Decorated Silver Nanowire-Reduced Graphene Oxide Aerogel Micro-Particle for Thermally Conductive Polymer Composites with Enhanced Flame Retardancy. *Macromol Rapid Commun*. 2022;43(18):e2200026.
doi: 10.1002/marc.202200026

47. Choi S G, Seok H J, Kim J, Kang J,Kim H K. Transparent and flexible passivation of MoS(2)/Ag nanowire with sputtered polytetrafluoroethylene film for high performance flexible heaters. *Sci Rep*. 2022;12(1):6010.
doi: 10.1038/s41598-022-09813-6

48. Zhou H W, Yang N, *et al.* Effects of CaCl, HCl, acetic acid or citric acid on dynamic mechanical performances and physicochemical properties of sodium alginate edible films. *Food Packaging Shelf*. 2022;34:100935.
doi: 10.1016/j.fpsl.2022.100935

49. Tai Y, Mulle M, Aguilar Ventura I,Lubineau G. A highly sensitive, low-cost, wearable pressure sensor based on

conductive hydrogel spheres. *Nanoscale*. 2015;7(35): 14766-14773.
doi: 10.1039/c5nr03155a

50. Wang C, Wang H, *et al.* On-skin paintable biogel for long-term high-fidelity electroencephalogram recording. *Sci Adv*. 2022;8(20):eabo1396.
doi: 10.1126/sciadv.abo1396

51. Zhang Z, Yang J, *et al.* A 10-micrometer-thick nanomesh-reinforced gas-permeable hydrogel skin sensor for long-term electrophysiological monitoring. *Sci Adv*. 2024;10(2):eadj5389.
doi: 10.1126/sciadv.adj5389

52. Qiao X, Cai Y, Kong Z, Xu Z,Luo X. A Wearable Electrochemical Sensor Based on Anti-Fouling and Self-Healing Polypeptide Complex Hydrogels for Sweat Monitoring. *ACS Sens*. 2023;8(7): 2834-2842.
doi: 10.1021/acssensors.3c00778